

Betelgeuse fainter in the sub-millimetre too:
an analysis of JCMT and APEX monitoring during the recent optical minimum

THAVISHA E. DHARMAWARDENA,¹ STEVE MAIRS,² PETER SCICLUNA,³ GRAHAM BELL,² IAIN McDONALD,^{4,5}
KARL MENTEN,⁶ AXEL WEISS,⁶ AND ALBERT ZIJLSTRA⁴

¹*Max-Planck-Institute for Astronomy, Königstuhl 17, 69117 Heidelberg, Germany.*

²*East Asian Observatory, 660 N. A'ohōkū Place, Hilo, HI 96720, USA*

³*European Southern Observatory, Alonso de Cordova 3107, Santiago RM, Chile*

⁴*Jodrell Bank Centre for Astrophysics, Alan Turing Building, University of Manchester, M13 9PL, UK*

⁵*Open University, Walton Hall, Milton Keynes, MK7 6AA, UK*

⁶*Max-Planck-Institute for Radio Astronomy, Auf dem Hügel 69, 53121 Bonn, Germany*

(Received May 8, 2020; Accepted June 14, 2020)

Submitted to ApJL

ABSTRACT

Betelgeuse, the nearest Red Supergiant star to us underwent an unusually deep minimum at optical wavelengths during its most recent pulsation cycle. We present submillimetre observations taken by the James Clerk Maxwell Telescope and Atacama Pathfinder Experiment over a time span of 13 years including the optical dimming. We find that Betelgeuse has also dimmed by $\sim 20\%$ at these longer wavelengths during this optical minimum. Using radiative-transfer models, we show that this is likely due to changes in the photosphere (luminosity) of the star as opposed to the surrounding dust as was previously suggested in the literature.

Keywords: Red supergiant stars (1375), Submillimetre astronomy (1647), Variable stars (1761), Time domain astronomy (2109)

1. INTRODUCTION

Massive stars ($M \geq 8 M_{\odot}$) are the main drivers of the chemical evolution in the Universe (Karakas & Lattanzio 2014). These stars explode as supernovae, releasing nuclear-processes material into the interstellar medium, chemically enriching the surrounding environment. Between the main sequence and their explosive demise, massive stars undergo enhanced mass loss; since the mass-loss rate exceeds the nuclear-burning rate, mass lost during these phases becomes the determining factor in their evolution from this point onwards, determining what kind of supernova they will become (e.g. Georgy 2012; Groh et al. 2013). For stars with masses $< 30 M_{\odot}$, the majority of this mass loss occurs as a red supergiant (RSG; van Loon 2013).

The mechanisms driving RSG mass loss remain debatable, but pulsations are believed to play a role in at least some cases (e.g. van Loon et al. 2005; Harper et al. 2009). High-amplitude, long-period pulsations carry stellar surface material into the interstellar medium with the aid of strong stellar winds (McDonald & Trabucchi 2019). These semi-regular pulsations have periods spanning $\sim 200 - 1000$ days are an inherent feature in evolved stars visible across a wide wavelength range (Höfner & Olofsson 2018).

Betelgeuse, the closest (152 ± 20 pc; van Leeuwen 2007) and best studied RSG, recently experienced an unusually deep minimum in its visual light curve (e.g. Guinan et al. 2019, 2020), which captured both professional and public interest. Four main scenarios were put forward for this dimming; i. a confluence of the short (~ 400 days) and long (~ 5 years) periods; ii. changes in known hot and cold spots on the stellar surface; iii. a large ejection of newly formed

dust along the line of sight; and more exciting iv. photospheric structural changes indicating an imminent supernova, which is now ruled out by the subsequent return to its original brightness.

Some of these hypotheses have been examined in recent literature. Optical imaging of the star with VLT/SPHERE showed a distinct change in the apparent shape of the photosphere between January and December 2019, with the southern half of the star substantially dimmer in the December observations¹. Levesque & Massey (2020) compared spectra from 2004 and 2020, and interpreted the moderate change in TiO bands as evidence for a lack of change in effective temperature based on comparison to 1D static models. Based on these considerations, the formation of a new dust cloud along the line of sight has emerged as the favoured hypothesis.

In this letter we present sub-millimetre (sub-mm) observations at 450 μm and 850 μm obtained by the Sub-mm Common User Bolometer Array 2 (SCUBA-2, Holland et al. 2013) instrument on the James Clerk Maxwell Telescope (JCMT). At these wavelengths, we avoid the effects of extinction along the line of sight, providing an unbiased probe of the emission of the star and its environs. Newly formed dust should be visible as increased emission, while the bright photosphere allows us to see any reduction in the overall luminosity of the star.

2. OBSERVATIONS AND DATA REDUCTION

JCMT/SCUBA-2 continuum observations were obtained as part of a director’s discretionary time program and an urgent queue program (project IDs M19BD002 and S20AP001, respectively; PI: Mairs) at 450 μm and 850 μm . Observations were carried out on 2020 Jan 23, Feb 16 and Mar 03 UT. These observations were approximately 11 minutes with $\tau_{225\text{GHz}} \lesssim 0.05$, reaching noise levels of 74–103 and 16–27 mJy/beam for 450 μm and 850 μm respectively. Five archival JCMT/SCUBA-2 observations obtained in 2012 and 2013 were also included for comparison, with integration times of ~ 6 minutes with $\tau_{225\text{GHz}} \lesssim 0.08$, reaching a noise level of 17–67 mJy/beam for 850 μm . The SCUBA-2 beam sizes at 850 and 450 μm are $\sim 13''$ and $\sim 7.9''$ respectively.

All observations were reduced using MAKEMAP (Chapin et al. 2013) with an edited version of the DIMMCONF-BRIGHT-COMPACT pipeline available in the JCMT reduction software STARLINK version 2018A (Currie et al. 2014). The modified parameters in the pipeline are as follows: NUMITER= -200 ; FLT.FILT_EDGE_LARGESCALE = 200; FLT.ZERO_CIRCLE = $2'$; AST.ZERO_CIRCLE = $2'$ and MAPTOL = 0.005. In addition to these parameters, each observation was convolved with a $7''$ Gaussian to ensure that all the flux was recovered (Dharmawardena et al. 2018; Dharmawardena et al. 2019b). Flux-calibration factors were applied following the East Asian Observatory (EAO) guidelines². The uncertainty on the absolute calibration of SCUBA-2 data is approximately 8% (Dempsey et al. 2013).

The CO J=3–2 transition line at 345.7 GHz contaminates SCUBA-2 850 μm observations (Drabek et al. 2012; Coudé et al. 2016; Dharmawardena et al. 2019a). To remove this contamination from our observations, we use an archival CO 3–2 staring observation obtained from the JCMT/Heterodyne Array Receiver Program (HARP) instrument on 2013 December 29. The measured CO 3–2 contribution to the SCUBA-2 point source flux is 0.033 Jy, for the half-power bandwidth of SCUBA-2 of 35 GHz. The upper energy level of the CO 3–2 is ≈ 33 K above the ground state, meaning that it samples the bulk gas in the envelope and hence we do not expect it to be strongly affected by variations in the temperature or luminosity of the star.

The full list of observations is presented in Table 1. Further, the SCUBA-2 data are complemented with archival 870 μm data obtained with the Large APEX Bolometer Camera (Siringo et al. 2009) which is operated on the Atacama Pathfinder Experiment submillimetre telescope (APEX), also shown in the same table. The APEX/LABOCA 870 μm observations of Betelgeuse were conducted between 2007 December and 2017 September. All observations were carried out using standard raster-spiral observations (Siringo et al. 2009) under good weather conditions (PWV= 0.6 – 1.4 mm). Integration times were between 180 and 750 seconds. Flux calibration was achieved through observations of Mars, Uranus, Neptune and secondary calibrators and is typically accurate within 8.5% rms. The atmospheric attenuation was determined via skydips every 2hr and from independent data from the APEX radiometer, which measures the line-of-sight water-vapour column every minute. The data were reduced and imaged using the BoA reduction package as detailed in Weiß et al. (2009). LABOCA’s central frequency and beam size are 345 GHz and $19.2''$. Fluxes were derived from the peak flux densities on the maps after smoothing the data with a Gaussian with a FWHM of $12''$. Resulting noise levels are between 10 and 30 mJy/beam.

¹ see the recent ESO Photo release <https://www.eso.org/public/news/eso2003/>, data from M. Montarges

² <https://www.eaoobservatory.org/jcmt/instrumentation/continuum/scuba-2/calibration/>

Table 1. Table of fluxes

MJD	UT Date	SCUBA-2 850 flux (Jy)	SCUBA-2 450 flux (Jy)	LABOCA 870 flux (Jy)
54458	2007-12-24	–	–	0.634
54791	2008-11-21	–	–	0.651
55132	2009-10-28	–	–	0.724
55517	2010-11-17	–	–	0.690
55654	2011-04-03	–	–	0.642
55792	2011-08-19	–	–	0.620
55966	2012-02-09	0.573	1.52	–
56191	2012-09-21	0.603	1.94	–
56214	2012-10-14	0.587	1.50	–
56280	2012-12-19	0.627	1.86	–
56318	2013-01-26	0.483	1.86	–
57668	2016-10-07	–	–	0.546
57874	2017-05-01	–	–	0.750
58007	2017-09-11	–	–	0.640
58871	2020-01-23	0.517	1.32	–
58895	2020-02-16	0.531	1.23	–
58911	2020-03-03	0.467	1.12	–

3. ANALYSIS AND DISCUSSION

3.1. Sub-mm flux variation

We derive the SCUBA-2 point source photometry for each observation by integrating under the point-spread function (PSF) scaled to the peak flux at sub-pixel precision. The PSF is generated by convolving the standard SCUBA-2 PSF consisting of two Gaussian components (Dempsey et al. 2013) and the $7''$ smoothing Gaussian. This approach is more effective in order to measure the compact-flux component, avoiding contamination by any negative bowing effects, and by the extended circumstellar-envelope component, which methods such as aperture photometry may cause. The pre-optical dimming (2012 – 2013) JCMT/SCUBA-2 850 μm fluxes are consistent with those derived by O’Gorman et al. (2017) using the ALMA main array at the same wavelength.

The JCMT/SCUBA-2 light curve, along with the archival APEX/LABOCA data, is shown in Fig.1. For comparison, the AAVSO³ optical (V band) light curve for the same date range is also shown here.

3.2. Modelling the lightcurve

To determine whether there is any evidence of variation in the sub-mm fluxes of Betelgeuse, we perform Bayesian inference by forward-modelling the fluxes with three different models and evaluate which one best-reproduces the fluxes simultaneously for SCUBA-2 850, SCUBA-2 450 and LABOCA. **Because the stellar signal is strong, we assume that the uncertainties of the fluxes are dominated by the systematic, uncorrelated scatter in the determination of the absolute calibration (Dempsey et al. 2013). The models we consider are:**

- C1:** constant flux. This model has three free parameters: c , the SCUBA-2 850 μm flux at 850 μm ; α_{450} , the ratio between the 450 and 850 fluxes; and α_{870} , the ratio between the SCUBA-2 850 and LABOCA 870 μm fluxes. These α parameters allow us to straightforwardly handle the conversion from the calibration of one instrument to another, which would otherwise inject additional uncertainty on the value of c .
- C2:** the behaviour is broken into two distinct epochs each with constant flux. Unlike model C1, only the α parameters are assumed to be fixed at all times. There are then three other parameters, t_{break} , the date at which the behaviour changes, and c and c' , the (otherwise constant) SCUBA-2 850 μm flux before and after t_{break} , respectively.

³ <https://www.aavso.org>

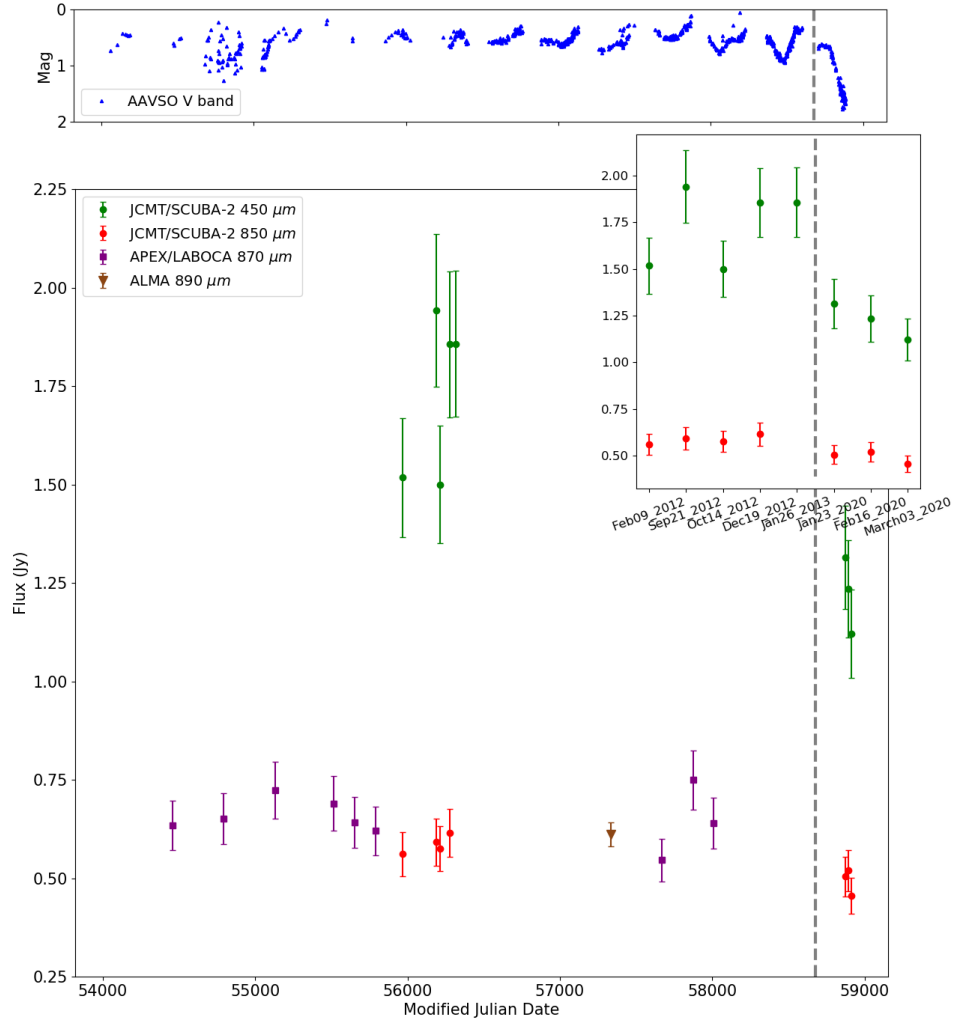


Figure 1. Lightcurves of Betelgeuse for the last fifteen years: The top panel shows the AAVSO optical (V band) light curve; The bottom panel shows the JCMT/SCUBA-2 450 μm (green points) and 850 μm (red points) light curve constructed using both archival and newly obtained observations. Here we also show the the APEX/LABOCA 870 μm light curve (purple squares) obtained from archival data. While not used in the fitting we also show the single ALMA 890 μm data point (brown triangle) from O’Gorman et al. (2017), to illustrate the consistency. The grey dashed line indicates the beginning of the dimming of the recent pulsation cycle. The inset panel shows a zoomed in version of the JCMT/SCUBA-2 light curve with the corresponding UT date for each observation. **All error bars indicate 1- σ uncertainties including the uncertainty on the absolute calibration.**

L: the flux varies linearly with time, with all bands following the slope. This is similar to model C1, except that an additional parameter m is added so that the fluxes are proportional to $mt + c$. This effectively assumes that the fractional rate of change at each band is the same.

In the absence of further constraints, the priors on all parameters are assumed to be flat, drawn from uniform random distributions that cover the required ranges, listed in Table 2.

We now have a model-selection problem including multiple comparisons. To identify the most appropriate model of the three, we must compute Bayes’ factors (K) for each comparison. **The Bayes factor provides a way to select between families of models by considering the total evidence (or integrated likelihood) over the whole prior volume and comparing the ratio of evidences for different families of models.** This requires that we have a reliable way of estimating the *evidence*, Z for each model (for further details on Bayes’ factors, see e.g. Goodman 1999a,b; Morey et al. 2016). To do this, we use the Python nested-sampling package DYNESTY, which supports dynamic nested sampling, allowing optimisation for either evidence estimation or posterior exploration

Table 2. Results of fitting using nested sampling

Model	$\ln Z$	α_{870}	α_{450}	c [Jy]	c' [Jy]	m	t_{break} MJD
C1	-36.11 ± 0.06	1.23 ± 0.05	2.73 ± 0.13	0.525 ± 0.015	–	–	–
C2	-29.24 ± 0.07	1.15 ± 0.06	2.81 ± 0.13	0.567 ± 0.018	0.466 ± 0.021	–	58320^{+380}_{-900}
L	-44.84 ± 0.11	1.15 ± 0.05	2.79 ± 0.13	2.22 ± 0.41	–	$(-2.96 \pm 0.72) \times 10^{-5}$	–
Priors	–	0 – 2	0 – 10	C1, C2: 0 – 1 L: 0 – 100	0 – 1	–3 – 3	56000 – 59000

(Skilling 2004, 2006; Higson et al. 2019; Speagle 2020). For each model, we conduct two runs, one optimised to estimate the evidence for the model selection, and the other optimised to evaluate the posterior and hence provide parameter estimates. All runs used 1500 initial live points and $\text{DLOGZ_INIT} = 0.01$. The estimated evidence and parameter values for each model are given in Table 2, along with their respective 1σ uncertainties.

Using the evidence computed using DYNesty, we now compute Bayes’ factors for each pair of models. Unlike frequentist approaches, Bayes’ factors automatically penalise models with more free parameters but do not privilege any model by considering it the null hypothesis. By assuming that all models are *a priori* equally likely, the Bayes factor collapses to the ratio of the evidences — the impact of this assumption is difficult to quantify, but this is a necessary starting point. The frequentist equivalent to the process would be to separately compare model C2 and L to C1, considering model C1 as the null hypothesis. However, this would require an additional penalty as we are performing multiple comparisons, while the use of Bayes factors avoids this issue.

The ratios of the evidence support model C2 over the other two models by a significant margin. For the comparison between C2 and C1, the Bayes’ factor $K = 710$, while the K comparison between C2 and L is $\sim 6 \times 10^6$. This represents *decisive* evidence in favour of model C2 (using the scale of e.g. Kass & Raftery 1995), suggesting not only that the sub-mm flux is variable but, crucially, that it is *lower* during the recent minimum than it was before. Given that the sub-mm emission is dominated by the star, this implies that the luminosity has decreased by nearly 20% (**a 3.6σ change**) and argues against models in which the recent optical dimming is caused by the formation of a new cloud of dust along the line of sight to the star, as increases in the dust mass *cannot* decrease the sub-mm flux as the dust emission at this wavelength is optically thin⁴.

To understand the role of dust versus the photosphere in the dimming across the optical–sub-mm wavelength range, we perform dust radiative-transfer modelling. We do not aim to quantitatively fit the observations, merely to qualitatively illustrate the trends that could be expected under different assumptions. Using the Monte Carlo radiative-transfer code HYPERION (Robitaille 2011), we compute models of a spherically-symmetric wind with constant outflow speed of 14 km s^{-1} (comparable to Loup et al. 1993). We use dust that consists of compact spherical grains composed of 30% alumina using optical constants from Begemann et al. (1997) and 70% Mg-Fe silicate for optical constants from Dorschner et al. (1995), with grain sizes from $0.1\text{--}1 \mu\text{m}$ following an MRN size distribution (Mathis et al. 1977). We use one million photons per iteration, which is sufficient as the shell is optically thin and spherically symmetric, with grid cells distributed logarithmically in radius. Using a dust mass-loss rate of $3 \times 10^{-9} M_{\odot} \text{ yr}^{-1}$ (e.g. Verhoelst et al. 2009) we achieve an acceptable fit to the optical–mid-infrared photometry. We then compute a second model, in which an additional shell of dust has been added between 2 and $4 R_{*}$, close to the observed dust-condensation radius (Haubois et al. 2019), which adds an additional 1 magnitude of optical extinction.

Comparing these two models (see Fig. 2), we see two distinctive features. Firstly, while the addition of new dust substantially changes the optical and infrared emission, it makes very little difference at wavelengths longer than $100 \mu\text{m}$. Secondly, Betelgeuse’s emission at sub-mm wavelengths is entirely dominated by the stellar photosphere, with small contributions from circumstellar dust and the radio **pseudo-photosphere (i.e. optically-thick excess radio emission whose size changes with wavelength, not included in our models)** (e.g. Richards et al. 2013; O’Gorman et al. 2017). The radio pseudo-photosphere, which dominates the spectrum at cm wavelengths and beyond (O’Gorman et al. 2015), clearly makes only a minor contribution at $850 \mu\text{m}$ and a negligible one at $450 \mu\text{m}$. Therefore, while we are unable to probe changes in dust mass at the level that would produce the optical dimming, it is clear

⁴ This is only true if the overall temperature structure does not change. In exceptional cases, it is possible to envisage the optical depth increasing sufficiently to lower the dust temperature such that the emission is reduced, but the radiative-transfer modelling shown in this section makes this a moot point in the case of Betelgeuse.

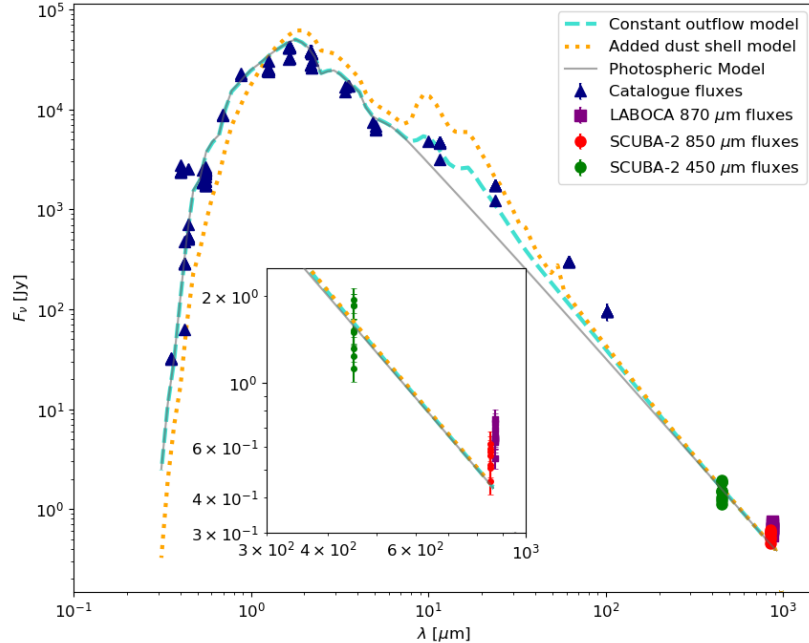


Figure 2. Radiative-transfer models (lines) compared with observations of Betelgeuse. Blue triangles show fluxes, taken from Vizier (listed in the online appendix, Table 3), and the green, red and purple points indicate the data from this work in the same colour scheme as Fig. 1. The blue dashed line represents a qualitative fit from HYPERION to the 0.3–30 μm photometry, and the orange dotted line a model that is identical other than the addition of an extra shell of dust from 2–4 R_* that produces 1 magnitude of V-band extinction and the grey solid line shows the underlying photospheric model at the same spectral resolution as the radiative-transfer models. The inset panel highlights the sub-mm fluxes from this work and the model flux in the same region.

that only changes in the photosphere can reproduce the sub-mm dimming – this would otherwise require that the dust emission or the radio pseudo-photosphere had completely disappeared. Using the same logic, we can exclude changes in the sub-mm line emission as a cause of the variations. Similar to CW Leo (Dharmawardena et al. 2019a), the CO contribution (the brightest line in these spectral regions) to the measured continuum is at the 5–10% level; short of all the molecular line emission disappearing, the continuum could not change by this amount.

Under the naïve assumption that the change in sub-mm flux corresponds to a change in temperature at constant radius, and that the original temperature was $T_{\text{eff}} = 3650$ K (the 2004 temperature from Levesque & Massey 2020), this would suggest a present value of 3450 K. Alternatively, this could be reconciled with the sub-mm data if starspots with $T_{\text{eff}} = 3250$ K cover 50% of the visible surface, or if spots with $T_{\text{eff}} = 3350$ K cover 70% of the visible surface. **Indeed, as can be seen in Fig. 3, all such scenarios would also be accompanied by a ~ 0.9 mag dimming in the V band, and are qualitatively similar to the 2020 spectrum of Levesque & Massey (2020), including the convergence of the spectra at the blue end with the warmer/2004 spectrum.** However, as a dynamic, non-equilibrium system, changes in temperature and the resulting molecular bands in pulsating stars may take some time to settle after a significant perturbation (e.g. McDonald & van Loon 2007; Lebzelter et al. 2010, 2014). Hence, one-dimensional models have difficulty capturing the observed behaviour and detailed 3D modelling is required. This might explain why the expected changes in TiO bands were not visible in the spectra of Levesque & Massey (2020), as it is typical to compare to static, one-dimensional models. If the change were instead due to a change in radius at constant temperature, the change in radius would be small ($\sim 10\%$), since $\Delta R \propto \sqrt{\Delta L}$.

4. CONCLUSIONS

We present new and archival sub-mm observations from JCMT/SCUBA-2 and APEX/LABOCA of the red supergiant Betelgeuse during its recent deep optical minimum. Modelling the sub-mm lightcurve shows that it is inconsistent

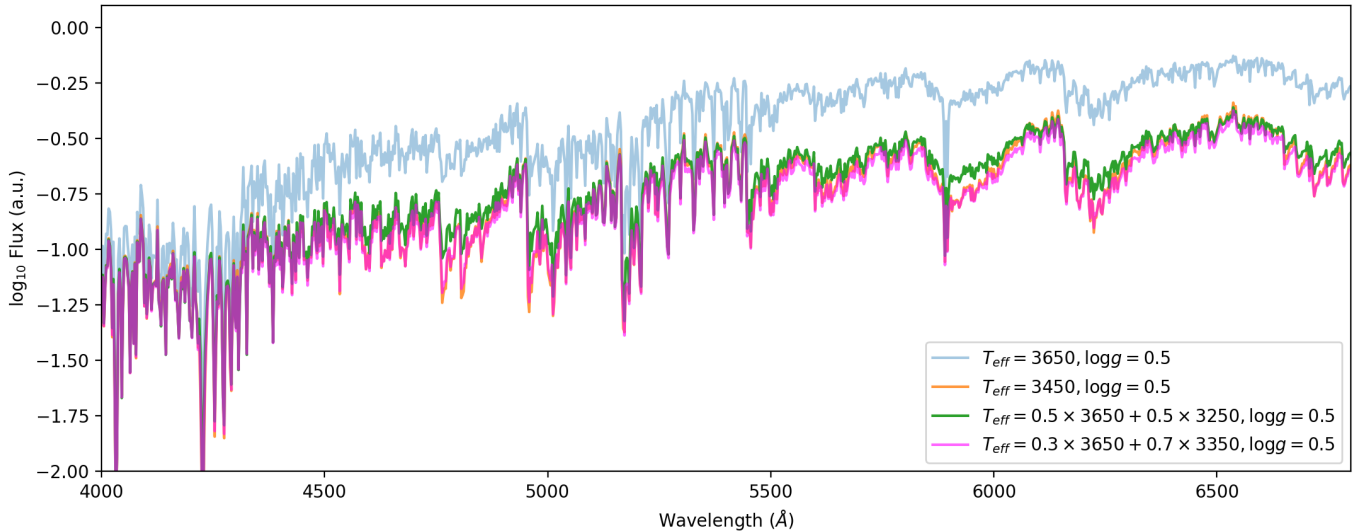


Figure 3. Comparison of optical (4000–7000 Å) model spectra (PHOENIX spectra (Husser et al. 2013) interpolated using the STARFISH package (Czekala et al. 2015; Czekala et al. 2018)) showing the influence of temperature changes and mixing of different temperature components, normalised so that the spectra are equal to one at the peak of the SED ($\sim 1.5 \mu\text{m}$) with the same wavelength sampling as in Levesque & Massey (2020), although not convolved with the line response function. All three scenarios outlined in the text have rather similar spectra, and are qualitatively similar to Figure 1 in Levesque & Massey (2020).

with the sub-mm flux remaining constant during the recent dimming. The models suggest that the sub-mm flux has declined by 20% compared to pre-dimming values. Radiative-transfer modelling shows that this cannot be caused by changes in the dust envelope, and therefore must reflect a change in the photosphere of the star. This 20% reduction in luminosity could take the form of a change in radius or temperature. The required change in radius would be small ($\sim 10\%$), while a change in temperature could be explained either through a $\sim 200 \text{ K}$ global change, or through the presence of spots $\sim 400 \text{ K}$ cooler covering $\sim 50\%$ of the visible surface.

ACKNOWLEDGEMENTS

We would like to thank Amelia Bayo for sharing LABOCA observations and Sarah Graves for help determining the CO contribution to SCUBA-2.

We acknowledge with thanks the variable star observations from the AAVSO International Database contributed by observers worldwide and used in this research.

This project is partially funded by the Sonderforschungsbereich SFB881 The Milky Way System of the German Research Foundation (DFG).

The James Clerk Maxwell Telescope is operated by the East Asian Observatory on behalf of The National Astronomical Observatory of Japan; Academia Sinica Institute of Astronomy and Astrophysics; the Korea Astronomy and Space Science Institute; the Operation, Maintenance and Upgrading Fund for Astronomical Telescopes and Facility Instruments, budgeted from the Ministry of Finance (MOF) of China and administrated by the Chinese Academy of Sciences (CAS), as well as the National Key R&D Program of China (No. 2017YFA0402700). Additional funding support is provided by the Science and Technology Facilities Council of the United Kingdom and participating universities in the United Kingdom and Canada. Program IDs: M19BD002, S20AP001, M10AEC30, M11BEC30, M12AEC05, M12BEC05 and M13BN01.

This publication is based on data acquired with the Atacama Pathfinder Experiment (APEX). APEX is a collaboration between the Max-Planck-Institut für Radioastronomie, the European Southern Observatory, and the Onsala Space Observatory. Observation project IDs M-79.F-0147-2007, M-081.F-1039-2008, M-083.F-0057-2009, M-085.F-0066-2010, C-098.F-9705A-2016, C-099.F-9720A-2017 and M-099.F-9529C-2017

REFERENCES

- Begemann, B., Dorschner, J., Henning, T., et al. 1997, *ApJ*, 476, 199
- Chapin, E. L., Berry, D. S., Gibb, A. G., et al. 2013, *MNRAS*, 430, 2545

- Coudé, S., Bastien, P., Kirk, H., et al. 2016, *MNRAS*, 457, 2139
- Currie, M. J., Berry, D. S., Jenness, T., et al. 2014, in *Astronomical Society of the Pacific Conference Series*, Vol. 485, *Astronomical Data Analysis Software and Systems XXIII*, ed. N. Manset & P. Forshay, 391
- Czekala, I., Andrews, S. M., Mandel, K. S., Hogg, D. W., & Green, G. M. 2015, *ApJ*, 812, 128
- Czekala, I., gully, Gullikson, K., et al. 2018, *iancze/Starfish: ca. Czekala et al. 2015 release w/ Zenodo*, , , doi:10.5281/zenodo.2221006. <https://doi.org/10.5281/zenodo.2221006>
- Dempsey, J. T., Friberg, P., Jenness, T., et al. 2013, *MNRAS*, 430, 2534
- Dharmawardena, T. E., Kemper, F., Wouterloot, J. G. A., et al. 2019a, *MNRAS*, 489, 3492
- Dharmawardena, T. E., Kemper, F., Scicluna, P., et al. 2018, *Monthly Notices of the Royal Astronomical Society*, 479, 536. <http://dx.doi.org/10.1093/mnras/sty1422>
- Dharmawardena, T. E., Kemper, F., Srinivasan, S., et al. 2019b, *MNRAS*, 489, 3218
- Dorschner, J., Begemann, B., Henning, T., Jaeger, C., & Mutschke, H. 1995, *A&A*, 300, 503
- Drabek, E., Hatchell, J., Friberg, P., et al. 2012, *MNRAS*, 426, 23
- Georgy, C. 2012, *A&A*, 538, L8
- Goodman, S. N. 1999a, *Annals of Internal Medicine*, 130, 995. <https://doi.org/10.7326/0003-4819-130-12-199906150-00008>
- . 1999b, *Annals of Internal Medicine*, 130, 1005. <https://doi.org/10.7326/0003-4819-130-12-199906150-00019>
- Groh, J. H., Meynet, G., & Ekström, S. 2013, *A&A*, 550, L7
- Guinan, E., Wasatonic, R., Calderwood, T., & Carona, D. 2020, *The Astronomer's Telegram*, 13512, 1
- Guinan, E. F., Wasatonic, R. J., & Calderwood, T. J. 2019, *The Astronomer's Telegram*, 13341, 1
- Harper, G. M., Richter, M. J., Ryde, N., et al. 2009, *ApJ*, 701, 1464
- Haubois, X., Norris, B., Tuthill, P. G., et al. 2019, *A&A*, 628, A101
- Higson, E., Handley, W., Hobson, M., & Lasenby, A. 2019, *Statistics and Computing*, 29, 891
- Höfner, S., & Olofsson, H. 2018, *A&A Rv*, 26, 1
- Holland, W. S., Bintley, D., Chapin, E. L., et al. 2013, *MNRAS*, 430, 2513
- Husser, T. O., Wende-von Berg, S., Dreizler, S., et al. 2013, *A&A*, 553, A6
- Karakas, A. I., & Lattanzio, J. C. 2014, *PASA*, 31, e030
- Kass, R. E., & Raftery, A. E. 1995, *Journal of the American Statistical Association*, 90, 773. <https://www.tandfonline.com/doi/abs/10.1080/01621459.1995.10476572>
- Lebzelter, T., Nowotny, W., Hinkle, K. H., Höfner, S., & Aringer, B. 2014, *A&A*, 567, A143
- Lebzelter, T., Nowotny, W., Höfner, S., et al. 2010, *A&A*, 517, A6
- Levesque, E. M., & Massey, P. 2020, arXiv e-prints, arXiv:2002.10463
- Loup, C., Forveille, T., Omont, A., & Paul, J. F. 1993, *A&AS*, 99, 291
- Mathis, J. S., Rumpl, W., & Nordsieck, K. H. 1977, *ApJ*, 217, 425
- McDonald, I., & Trabucchi, M. 2019, *MNRAS*, 484, 4678
- McDonald, I., & van Loon, J. T. 2007, *A&A*, 476, 1261
- Morey, R. D., Romeijn, J.-W., & Rouder, J. N. 2016, *Journal of Mathematical Psychology*, 72, 6, bayes Factors for Testing Hypotheses in Psychological Research: Practical Relevance and New Developments. <http://www.sciencedirect.com/science/article/pii/S0022249615000723>
- O’Gorman, E., Harper, G. M., Brown, A., et al. 2015, *A&A*, 580, A101
- O’Gorman, E., Kervella, P., Harper, G. M., et al. 2017, *A&A*, 602, L10
- Richards, A. M. S., Davis, R. J., Decin, L., et al. 2013, *MNRAS*, 432, L61
- Robitaille, T. P. 2011, *A&A*, 536, A79
- Siringo, G., Kreysa, E., Kovács, A., et al. 2009, *A&A*, 497, 945
- Skilling, J. 2004, in *American Institute of Physics Conference Series*, Vol. 735, *American Institute of Physics Conference Series*, ed. R. Fischer, R. Preuss, & U. V. Toussaint, 395–405
- Skilling, J. 2006, *Bayesian Anal.*, 1, 833. <https://doi.org/10.1214/06-BA127>
- Speagle, J. S. 2020, *MNRAS*, 493, 3132
- van Leeuwen, F. 2007, *A&A*, 474, 653. <https://doi.org/10.1051/0004-6361:20078357>
- van Loon, J. T. 2013, in *EAS Publications Series*, Vol. 60, *EAS Publications Series*, ed. P. Kervella, T. Le Bertre, & G. Perrin, 307–316
- van Loon, J. T., Cioni, M.-R. L., Zijlstra, A. A., & Loup, C. 2005, *A&A*, 438, 273
- Verhoelst, T., van der Zypen, N., Hony, S., et al. 2009, *A&A*, 498, 127
- Weiß, A., Kovács, A., Coppin, K., et al. 2009, *ApJ*, 707, 1201

APPENDIX

A. LITERATURE FLUXES USED FOR RADIATIVE-TRANSFER MODELLING

Table 3. Fluxes used in Fig. 2

Filter	Freq GHz	Flux Jy	Uncertainty Jy	Reference Vizier table
Johnson:U	849030	32.6		II/7A/catalog
Johnson:U	849030	32		II/7A/catalog
HIP:Hp	745750	2.37×10^3	50	I/239/hip_main
HIP:Hp	745750	2.77×10^3		V/137D/XHIP
HIP:BT	713280	286	2	I/239/hip_main
HIP:BT	713280	62.5		I/275/ac2002
Johnson:B	674900	2.55×10^3	2.8×10^2	IV/38/tic
Johnson:B	674900	517		II/7A/catalog
Johnson:B	674900	531		II/7A/catalog
Johnson:B	674900	507	9	I/305/out
Johnson:B	674900	707		V/137D/XHIP
Johnson:B	674900	507	8	V/145/sky2kv5
Johnson:B	674900	527		B/pastel/pastel
HIP:VT	563630	1.85×10^3	30	I/239/hip_main
Johnson:V	541430	1.93×10^3		II/122B/merged
Johnson:V	541430	2.47×10^3		II/7A/catalog
Johnson:V	541430	2.15×10^3		I/239/tyc_main
Johnson:V	541430	2.52×10^3		II/7A/catalog
Johnson:V	541430	1.91×10^3		II/21A/catalog
Johnson:V	541430	1.74×10^3		II/53/catalog
Johnson:V	541430	2.4×10^3		J/other/NatAs/4.03/lit
Johnson:V	541430	2.52×10^3		II/122B/merged
Johnson:V	541430	2.3×10^3		III/124/stars
Johnson:V	541430	2.47×10^3		B/pastel/pastel
Johnson:V	541430	2.65×10^3	60	IV/38/tic
Johnson:V	541430	2.4×10^3		I/239/hip_main
Johnson:R	432100	8.65×10^3		II/7A/catalog
Johnson:R	432100	8.89×10^3		II/7A/catalog
Johnson:I	341450	2.28×10^4		II/7A/catalog
Johnson:I	341450	2.22×10^4		II/7A/catalog
Johnson:J	239830	2.53×10^4	2.4×10^3	II/246/out
Johnson:J	239830	2.39×10^4		II/7A/catalog
Johnson:J	239830	2.55×10^4		II/7A/catalog
DIRBE:1.25	237320	3.06×10^4		J/ApJS/190/203/var
Johnson:H	183920	4.17×10^4	6.2×10^3	II/246/out
Johnson:H	183920	3.23×10^4		II/7A/catalog
Johnson:K	136890	3.68×10^4	6.3×10^3	II/246/out
Johnson:K	136890	2.62×10^4		II/7A/catalog
Johnson:K	136890	2.6×10^4		II/7A/catalog
DIRBE:2.2	134960	3.11×10^4		J/ApJS/190/203/var
Johnson:L	88174	1.7×10^4		II/7A/catalog
Johnson:L	88174	1.51×10^4		II/7A/catalog
DIRBE:3.5	85118	1.73×10^4		J/ApJS/190/203/var
DIRBE:4.9	61312	7.49×10^3		J/ApJS/190/203/var
Johnson:M	59601	6.41×10^3		II/7A/catalog
Johnson:M	59601	6.23×10^3		II/7A/catalog
Johnson:M	59601	6.9×10^3		II/7A/catalog
:=10um	29979	4.8×10^3		II/53/catalog
IRAS:12	25866	4.68×10^3	1.9×10^2	II/125/main
IRAS:25	12554	1.74×10^3	70	II/125/main
IRAS:60	4847.1	299	21	II/125/main
IRAS:100	2940.6	95.9	19	II/125/main